Relationship between Synoptic Weather Patterns and Topography on Snowfall in the Idaho Mountainous Regions during the SNOWIE Project

ZHIXING XIE,[a] KATJA FRIEDRICH,[a] SARAH A. TESSENDORF,[b] LULIN XUE,[b] SISI CHEN,[b] THEODORE WHITTOCK,[a] BART GEERTS,[c] AND KYOKO IKEDA[b]

[a] *Department of Atmospheric and Oceanic Sciences, University of Colorado Boulder, Boulder, Colorado*
[b] *Research Applications Laboratory, National Center for Atmospheric Research, Boulder, Colorado*
[c] *Department of Atmospheric Science, University of Wyoming, Laramie, Wyoming*

(Manuscript received 15 September 2023, in final form 10 May 2024, accepted 18 May 2024)

ABSTRACT: Snowpack melting is a crucial water resource for local ecosystems, agriculture, and hydropower in the Intermountain West of the United States. Glaciogenic seeding, a method widely used in mountain regions to enhance precipitation, has been subject to numerous field studies aiming to understand and validate this mechanism. However, investigating precipitation distribution and amounts in mountainous areas is complicated due to the intricate interplay of synoptic circulation patterns and local complex topography. These interactions significantly influence microphysical processes, ultimately affecting the amount and distribution of surface precipitation. To address these challenges, this study leverages Weather Research and Forecasting (WRF) Model simulations, providing high-resolution (900 m), hourly data, spanning the Payette region of Idaho from January to March 2017. We applied the self-organizing map approach to categorize the most representative synoptic circulation patterns and conducted a multiscale analysis to explore their associated environmental conditions and microphysical processes, aiming to assess the cloud seeding potential. The analysis identified four primary synoptic patterns: cold zonal flow (CZF), cold southwesterly flow (CSWF), warm zonal flow (WZF), and warm southwesterly flow (WSWF), constituting 21.3%, 23.1%, 30.0%, and 25.5%, respectively. CSWF and WSWF demonstrated efficiency in generating natural precipitation. These patterns were characterized by abundant supercooled liquid water (SLW) and ice particles, facilitating cloud droplet growth through seeder–feeder processes. On the other hand, CZF exhibited the least SLW and limited potential for cloud seeding, while WZF displayed a lower ice water content but substantial SLW in the diffusion/dendritic growth layer, suggesting a favorable scenario for cloud seeding.

SIGNIFICANCE STATEMENT: Understanding snowfall amounts and distribution in the mountains and how it is linked to topography, synoptic flow, and microphysical processes will help in the development of effective strategies for cloud seeding operations, managing runoff, reservoir, and mitigating flood risks, garnering substantial interest from stakeholders and the government agencies.

KEYWORDS: Cloud microphysics; Cloud water/phase; Cloud seeding; Mesoscale models; Clustering

1. Introduction

In the Intermountain West of the United States, mountain snowpack holds a substantial volume of water that accumulates during the winter and gradually melts in warmer months. This process serves as a crucial water source for many western states of the United States, playing a vital role in supporting local ecosystems, water supply, agriculture, and hydropower. Understanding snowfall amounts and distribution in the mountains and how it is linked to topography, synoptic flow, and microphysical processes will help in the development of effective strategies for managing runoff, reservoir, and mitigating flood risks, garnering substantial interest from stakeholders and the government agencies. However, forecasting precipitation over complex terrain remains a formidable challenge. This challenge arises from a grasp of the intricate interactions between coupled multiscale microphysical and thermodynamical processes, topography, and their collective impact on surface precipitation (Kirshbaum et al. 2018; Lehner and Rotach 2018; Serafin et al. 2020). In this study, we employ the self-organizing map approach to analyze 900-m resolution, hourly simulations generated by the Weather Research and Forecasting (WRF) Model. These simulations, conducted between January and March 2017, specifically focused on the Payette Mountains of Idaho and the period of the Seeded and Natural Orographic Wintertime Clouds: the Idaho Experiment (SNOWIE). Our objective is to investigate the interplay of synoptic weather patterns, mesoscale microphysical and thermodynamical processes in complex terrain during SNOWIE, and how they influence the suitability for cloud seeding, as well as snowfall amount and distribution.

Significant precipitation events in the interior western United States have been linked to specific moisture pathways and synoptic weather patterns (Rutz et al. 2015; Swales et al. 2016; Zhang et al. 2022). In the context of SNOWIE (January–March 2017), the three moisture pathways were dominant during snowstorms: Sierra-blocked, southwest, and zonal

Supplemental information related to this paper is available at the Journals Online website: https://doi.org/10.1175/JAMC-D-23-0170.s1.

Corresponding author: Zhixing Xie, Zhixing.Xie@colorado.edu

DOI: 10.1175/JAMC-D-23-0170.1

flow (Cann and Friedrich 2020). They employed the NOAA Hybrid Single-Particle Lagrangian Integrated Trajectory (HYSPLIT) model to trace the backward trajectory of moisture pathways entering the Payette Mountains. These synoptic conditions play a crucial role in transporting water vapor into the area and determining surface snowfall amounts and distribution. In a similar study, Tessendorf et al. (2019) classified these 24 SNOWIE cases into four synoptic patterns, i.e., atmospheric river, northwest flow, orographic cloud, and convective cloud events based on 500-hPa geopotential height and flow structure. While observational and numerical studies have delved into the microphysical and thermodynamical characteristics of cloud seeding (e.g., French et al. 2018; Friedrich et al. 2020, 2021; Xue et al. 2022), only a few studies have investigated the favorable environmental and microphysical conditions for anthropogenic cloud seeding operations over multiple years (Mazzetti et al. 2021, 2023; Tessendorf et al. 2020). These seasonal analyses assessed seeding potential by examining whether the atmospheric conditions met the basic seeding criteria, such as a threshold for liquid water content within a specific temperature range. However, it is important to note that these criteria are subjective, and the influence of synoptic and topographic factors on water vapor transportation and amounts of supercooled liquid water have not been thoroughly considered in these analyses.

To assess the potential of cloud seeding, it is essential to first understand the formation and enhancement of natural precipitation. This understanding is crucial because the effectiveness of seeding tends to be less pronounced when natural precipitation processes are already operating efficiently (Xue et al. 2013). In the mountains, precipitation enhancement occurs due to orographic lifting, a cooling mechanism that promotes water vapor condensation and cloud formation (Napoli et al. 2019; Yu et al. 2022). As the moist air is forced to rise over elevated terrain, it cools and condenses, giving rise to cloud formation and, depending on the efficiency of cloud microphysical processes, subsequently precipitation. This process is particularly effective in enhancing precipitation on the windward side of mountains (Lin 2007). A microphysical process influencing cloud droplet growth and precipitation is the seeder–feeder effect. The seeder–feeder mechanism occurs when ice crystals, acting as seeds, descend from the upper cloud into a lower-lying cloud containing supercooled liquid water (SLW) or a mix of ice and SLW. Within the mixed-phased cloud, these ice crystals undergo further growth, facilitated by processes like riming, dendritic growth, or vapor deposition. The lower-lying liquid or mix-phase cloud functions as a "feeder," providing the water necessary for the continued growth of the descending ice crystals (Fernández-González et al. 2015). This process shares similarities with natural aerosols that act as ice-nucleating particles, initiating heterogeneous ice formation in mixed-phase clouds (Yang et al. 2021). Acknowledged for its significant impact, the seeder–feeder mechanism plays a pivotal role in orographic enhancement (Purdy et al. 2005) and is closely associated with the enhancement of heavy precipitation events (Rössler et al. 2014). In this study, our focus will be on analyzing cloud microphysical processes in complex terrain and investigating their influence on the distribution and quantity of precipitation.

Understanding the factors influencing cloud formation and orographic precipitation involves considering both mesoscale processes that directly impact cloud development and synoptic-scale water vapor transport, which governs the moisture supply. A well-established approach to study synoptic-scale water vapor transport involves categorizing the synoptic-scale circulation patterns and identifying the ones most closely linked to precipitation distribution and amounts (Ohba et al. 2015; Zhang et al. 2022). In recent times, the self-organizing map (SOM) approach, an unsupervised machine learning technique, has gained popularity for weather pattern classification compared to traditional clustering methods like *k*-means (e.g., Baiman et al. 2023). The SOM approach has proven to be effective at capturing variations in large-scale dynamics and transitions of weather systems. It has been widely used to explore the relationship between weather patterns and precipitation as a pattern recognition method. For example, Swales et al. (2016) utilized SOM to investigate the connections between water vapor transportation and extreme precipitation events in the intermountain west regions. Wang et al. (2022) applied SOM to 700-hPa geopotential height anomalies to establish a connection between synoptic patterns, cloud properties, and regional circulations over Southeastern Texas. Zhang et al. (2022) identified the most representative circulation patterns conducive to high-intensity precipitation events in China Henan Province through SOM clustering. However, it is worth noting that while many studies focus on determining moisture pathways and associated flow patterns, they often overlook the kinematic and thermodynamic effects of topography. These effects are crucial factors influencing orographic precipitation in complex terrain.

In this study, we utilized high-resolution (900-m domain nested within 2700-m domain) simulations from the WRF Model driven by data from the fifth major global reanalysis produced by ECMWF (ERA5). These simulations covered the period from January to March 2017, which coincided with the SNOWIE field campaign. Previous research related to SNOWIE primarily focused on examining the effects of cloud seeding on cloud microphysics and surface snowfall (French et al. 2018; Friedrich et al. 2020, 2021), investigating the role of vertical motion and supercooled liquid generation using aircraft observations (Geerts et al. 2023; Zaremba et al. 2022a,b; Heimes et al. 2022), or validating for the state-of-art seeding parameterizations for some well-observed SNOWIE cases (Xue et al. 2022). A recent study by Warms et al. (2023) employed the same 0.9-km resolution WRF simulations to examine snowfall events in the Payette Mountains from 1 October 2016 to 31 April 2017. Their research focused on understanding the variability of snowfall accumulation and distribution during the winter season. Their study discussed conditions conducive to efficient snowfall and successful cloud seeding, characterized by elevated levels of elevated supercooled liquid water. However, their study did not delve into the influence of topography and synoptic circulation during these snowfall events. Therefore, our study stands out by utilizing seasonal simulation data and employing a SOM technique to establish connections between environmental characteristics, such as terrain effects, water vapor transport, and cloud microphysics, in relation to the

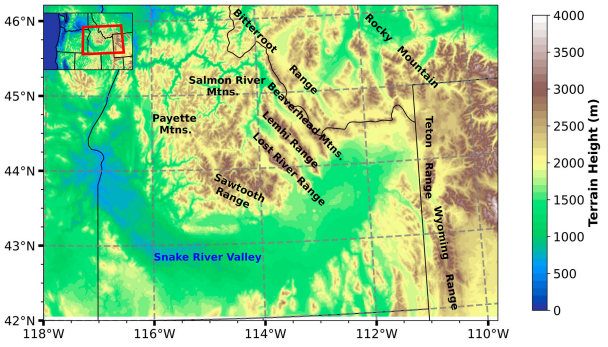

FIG. 1. Topographic map of the area covered by the 900-m WRF simulations (inner domain or domain 2) highlighting topographic features discussed in the text. The domain covered by the 2700-m WRF Model simulations (outer domain or domain 1) is shown in the inset in the upper-left corner, with the red box outlining the boundary of the inner domain.

distribution and amounts of orographic precipitation. There is a significant ongoing discussion regarding the feasibility and cost-effectiveness of cloud seeding. The question at hand is how often we encounter favorable conditions for seeding during a given season. Currently, all snow events are seeded in the western United States. However, if we get a better understanding of the spatiotemporal variability of natural microphysics, we might be able to better target storms that are favorable for cloud seeding and avoid overseeding. While this might vary from year to year, currently, there is a lack of studies addressing this issue. However, we acknowledge that this kind of study needs to be extended over multiple years to better understand seasonal variabilities.

This study aims to address three key questions related to the SNOWIE field campaign: 1) What are the typical synoptic circulation patterns, and how do these patterns of water vapor transport correlate with precipitation amounts and distributions? 2) What are the kinematic, thermodynamic, and microphysical processes at play, and how are they related to the underlying terrain and snowfall? and 3) Which synoptic scenarios offer the most favorable environmental conditions for glaciogenic cloud seeding?

This paper is organized as follows: In section 2, we provide an overview of the datasets and methods utilized in this study. Section 3 presents the results of our SOM analysis, highlighting moisture transport and precipitation distribution and amounts within the SOM categories. We delve into an analysis of precipitation efficiency by examining ice water and water paths as well as vertical velocity associated with these SOM patterns. Finally, in section 4, we summarize our findings, draw conclusions, and discuss the potential for glaciogenic seeding under four different synoptic circulation scenarios during SNOWIE.

2. Data and methods

a. Datasets

To investigate synoptic flow patterns over Idaho during the period from January to March 2017, we employed data from the ERA5 (Hersbach et al. 2020) as input for an SOM model.

TABLE 1. Selection of model configurations for the 2700- and 900-m WRF Model simulations. The outline of the domains is shown in Fig. 1.

	2700-m domain 1	900-m domain 2
Number of horizontal grid points	400 × 630	540 × 810
Driving data	ERA5	
Vertical coordinate	81 terrain-following ETA levels	
Land surface model	Noah MP	
Radiation	RRTMG	
Planetary boundary layer scheme	MYNN	
Microphysics	Thompson–Eidhammer	
Aerosol impact	aer_opt = 3	

We utilized hourly ERA5 data, featuring a horizontal resolution of about 27 km (0.25° × 0.25°), covering the northwestern United States and Pacific Ocean (105°–140°W, 30°–55°N; Fig. 1). Our SOMs were trained on geopotential heights at 700 hPa. For each specific SOM node, we derived average fields based on the hourly ERA5 data of integrated water vapor transport (IVT), horizontal wind at 700 hPa, and temperature at 700 hPa.

To investigate the mesoscale interactions between orographic flow, terrain, and precipitation within the Payette Mountain region, we used the results from the SOM model trained on ERA5 data. The specific SOM nodes trained with ERA5 data were then applied to the hourly, higher-resolution (900 m) WRF Model simulations for the same time period but focusing on the Payette Mountains of Idaho (Fig. 1). This approach is justified as the WRF Model simulations are initiated/nudged every hour with the ERA5 data. Moreover, the comparison of 700-hPa geopotential height patterns from ERA5 and WRF Model simulations, as based on the SOM model, demonstrated good agreement (more discussion can be found in section 3a).

The details of the WRF Model configuration are listed in Table 1. For the 900-m WRF Model simulation, no parameterization scheme is used to represent cumulus clouds as convection is explicitly resolved. This means that all precipitation was generated directly from a microphysics scheme at the grid scale. The microphysics scheme used here is the aerosol-aware Thompson–Eidhammer scheme (Thompson and Eidhammer 2014), which is a revised version of the Thompson scheme (Thompson et al. 2004, 2008). Originally designed for wintertime clouds and precipitation, the Thompson–Eidhammer scheme has now been widely applied to study the vertical distribution of hydrometeors (Han et al. 2013; Song and Sohn 2018).

b. SOM method

The SOM technique leverages a sophisticated neural network algorithm that utilizes unsupervised learning to identify generalized patterns in data. By clustering similar data records and arranging them into a two-dimensional map, this approach effectively reduces the dimensionality of vast datasets. Consequently, large multidimensional datasets are transformed into more easily comprehensible forms. While the SOM algorithm may be classified as a clustering technique, it

stands out from other clustering methods as it does not require preconceived notions about data distribution and instead relies on an iterative training process. The completed two-dimensional array of patterns (SOM) comprehensively displays the full continuum of states present in the training dataset. This array is strategically arranged to group similar patterns in proximity and dissimilar patterns on opposite corners, facilitating the examination of interpattern relationships. A detailed description of the SOM algorithm has been provided by Kohonen (1990). The SOM technique has been widely utilized to organize synoptic weather patterns to study how synoptic flow affects local precipitation in various geographical regions (Swales et al. 2016; Wang et al. 2022; Zhang et al. 2022).

The objective of this paper was to study the differences in microphysics and precipitation patterns for different synoptic weather patterns. Midlevel water vapor transport plays a crucial role in cloud microphysics and precipitation generation, particularly in the western United States. Cann and Friedrich (2020) utilized the 700-hPa level to track airmass trajectory through the use of HYSPLIT and classified them into four categories during SNOWIE. Tessendorf et al. (2019) classified the 24 SNOWIE cases into four categories based on the 500-hPa geopotential height and flow structure. Therefore, in this study, we utilize geopotential height fields at 700 and 500 hPa, as input data to train our SOM model. The general procedure applied includes the following: 1) Weight initialization: The SOM model is initialized with weights to each connection with the input data. These weights represent the relationship of the mapping neuron with the input vector. 2) Best matching neuron selection: We determined the best matching neuron by calculating the Euclidean distance between the neuron and the input data, selecting the neuron with the smallest distance. 3) Weight updating: An iterative process is used to update the weights of the neurons within the defined neighborhood radius, making them more similar to the input vector. 4) Model evaluation: The performance of the SOM model is assessed, and the optimal number of the nodes for the best-performing SOM architecture is determined (Wang et al. 2022). To build the SOM model, we employed the MiniSom software package, a widely used Python library (Vettigli 2018). We used the ERA5 dataset, as described in section 2a, as the input data for training the SOM model.

When utilizing the SOM technique, a crucial decision to consider is the number of patterns generated by the algorithm. Opting for a smaller number of patterns allows for distinct differences in features to be easily observed and for the SOM to be clearly visualized. However, this approach may result in generalized patterns that fail to identify features of infrequent events. On the other hand, larger SOM arrays enable finer distinctions between each pattern and can effectively separate similar patterns with important minor variations. Nevertheless, using a large SOM array may make it difficult to visualize all patterns and may also affect representativeness due to the limited number of events associated with each pattern. To determine the SOM configuration used in this study, we generated multiple sets of SOMs by varying neighborhood radius, learning rates, and the

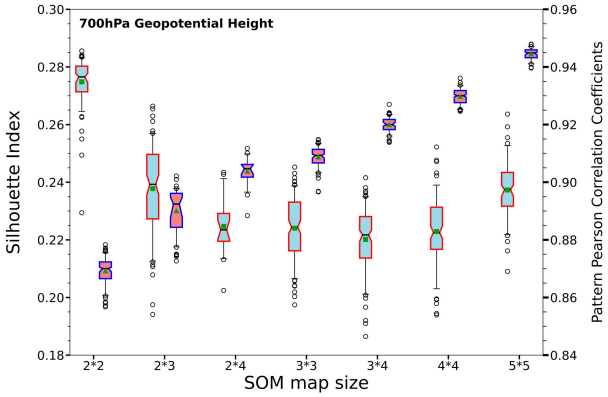

FIG. 2. Box-and-whisker plots of the SI (light blue with red edges) and the PPCCs (light red with blue edges). The plots represent evaluation metrics for the SOM models trained using 700-hPa geopotential height under different configurations.

number of SOM nodes, following the approach used by Udy et al. (2021) and Wang et al. (2022). Initially, we defined a range for each parameter and tested different combinations of parameters within these ranges. Specifically, we considered a neighborhood radius ranging from 1 to 2 in increments of 0.1 and a learning rate ranging from 0.4 to 1.7 with 0.1 intervals and explored seven different SOM map sizes (2×2, 2×3, 2×4, 3×3, 3×4, 4×4, 5×5) for both the 700-hPa (Fig. 2) and the 500-hPa geopotential heights (Fig. S1 in the online supplemental material).

To assess the classification performance, we used two metrics: the silhouette index (SI; Rousseeuw 1987) and the pattern Pearson correlation coefficients (PPCCs; Gibson et al. 2017; Udy et al. 2021). These metrics are commonly used to evaluate the consistency and similarity among clusters of input data. They both have a maximum value of up to 1, with higher values indicating better model performance. When evaluating the 700-hPa geopotential height SOM model, we observed that the PPCC monotonically increased within a range of 0.87–0.95 (Fig. 2). On the other hand, the SI initially decreased from 0.28 to 0.22 and then gradually increased from 0.22 to 0.24 as the node size increased (Fig. 2). The SI reached its highest value for a 2×2 node configuration, while the PPCC achieved its peak with a 5×5 node. Given that SOM structures showed relatively good performance according to the PPCC (all above 0.86), we gave more weight to the improvement of SI when selecting the number of nodes. Additionally, choosing an optimal SOM structure involves determining the necessary number of nodes to accurately represent relevant circulation types for analysis, while also ensuring a manageable number of nodes for effective result visualization (Cassano et al. 2015). Therefore, we considered the 2×2 SOM structure as the most appropriate architecture. Furthermore, our evaluation indicated that the SOM model using 700-hPa geopotential height field as input data (Fig. 2 for 700-hPa maps) outperformed the model using 500-hPa geopotential height (Fig. S1 for 500-hPa maps). Consequently, we utilized the 700-hPa geopotential height as input data and implemented the 2×2

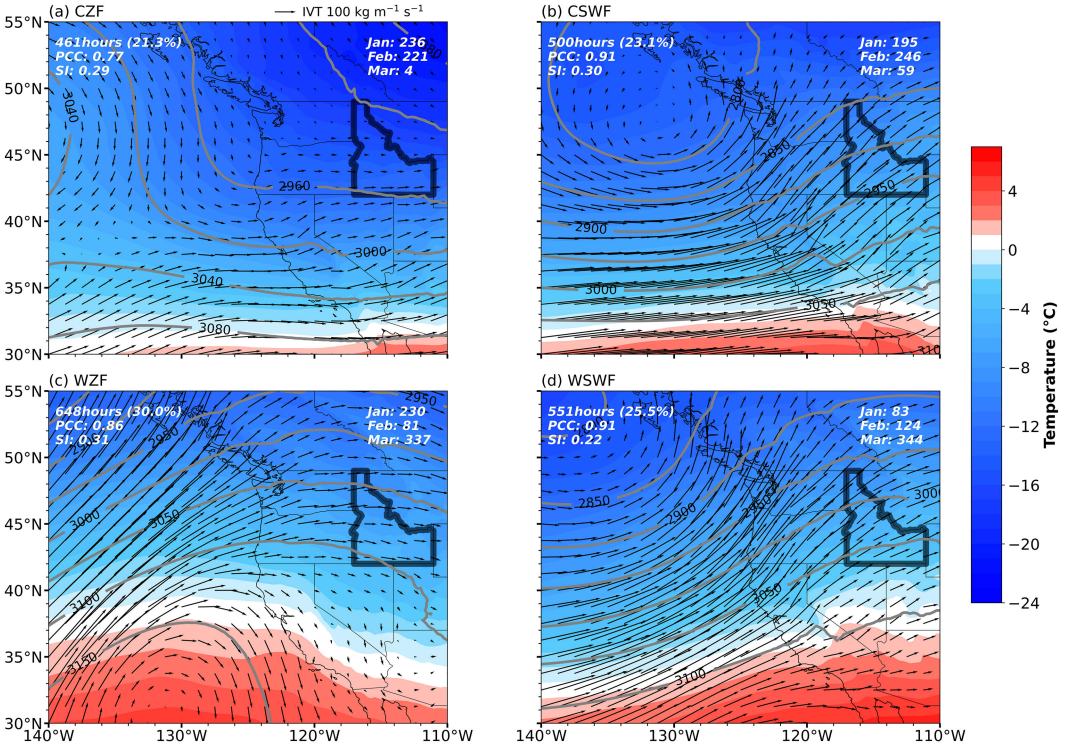

FIG. 3. Four synoptic regimes over the western United States represented by the SOM model: (a) CZF, (b) CSWF, (c) WZF, and (d) WSWF. The patterns show geopotential height (solid gray lines), temperature (color coded) at 700 hPa, and water vapor flux integrated between the surface and 300 hPa (IVT; arrows). The total hours included in the SOM, PPCC, and SI are indicated in the upper left corner. The hours per month are shown in the upper-right corner. State borders are marked with solid black lines, with the state of Idaho highlighted in bold.

SOM node structure to train our model, selecting it as the optimal configuration for the following analysis.

c. *Moisture transport and hydrometer content*

The supercooled liquid water path (SLWP) and ice water path (IWP) were calculated to analyze the horizontal distribution of integrated values of SLW and ice-phased water content. The calculation of SLWP and IWP was modified based on the definition of liquid water path provided by the American Meteorological Society (2020). Specifically, we replaced the liquid water mixing ratio with supercooled liquid water for temperature < 0°C to calculate the supercooled liquid water mixing ratio and ice-phased water mixing ratio. To investigate the water vapor supply, we plotted the IVT for the four SOM node patterns. IVT was calculated by integrating water vapor transport from the surface (p_s) up to 300 hPa (p_t) using the formula as follows:

$$\mathrm{IVT} = -\frac{1}{g}\int_{p_s}^{p_t} qV\,dp, \tag{1}$$

where g is the gravitational acceleration (9.8 m s^{-2}), V is the magnitude of wind (m s^{-1}), q represents the mean specific humidity (kg kg^{-1}) within each integrated layer, and dp denotes the pressure (hPa) difference between each integrated layer.

3. Results

a. *Synoptic weather regimes*

The SOM model classified hourly geopotential height maps at 700 hPa almost equally into four distinct patterns, each containing about 461–646 h of data, each node accounting for 21%–30% of the entire dataset (Fig. 3). In the CZF pattern (Fig. 3a), Idaho was located southwest of a low pressure system that funnels cold air from higher latitudes into the region, resulting in westerly winds over the Payette Mountains. At 700 hPa, temperature T ranged between −18° and −12°C and vertically integrated water vapor flux (IVT) varied between 22 and 54 kg m^{-1} s^{-1} (Fig. 4a). CZF represented the coldest and driest case of all, primarily occurring in January and February (221–236 h) and rarely in March (4 h). In the CSWF pattern (Fig. 3b), a cyclone was situated off the West Coast of the United States over the Pacific Ocean, transporting an ample amount of moisture from low latitudes to Idaho (IVT $>$ 90 kg m^{-1} s^{-1}; Fig. 4b). Temperatures at 700 hPa range from −10° to −4°C. CSWF was predominant in February (246 h), followed by 195 h in January and 59 h in March. The WZF pattern (Fig. 3c) was characterized by a ridge of high pressure off the southwestern coast of California over the Pacific Ocean, resulting in warm temperatures (from −9.5° to −4°C at 700 hPa; Fig. 4c) and zonal upstream winds over Idaho. IVT ranged between 50 and 88 kg m^{-1} s^{-1} (Fig. 4c). This

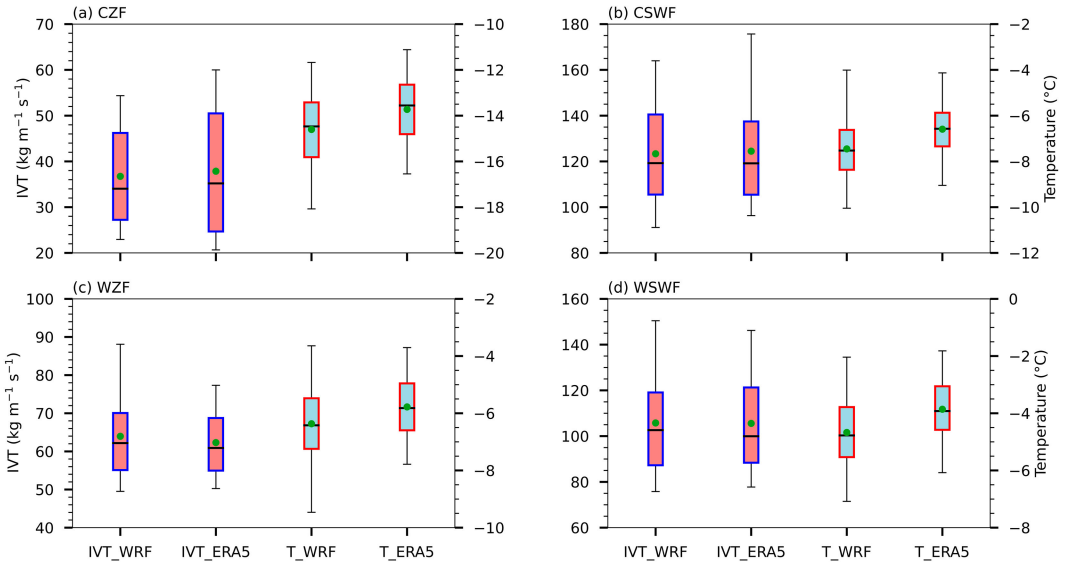

FIG. 4. Box-and-whisker plots of integrated water vapor flux (IVT; light red with blue edges) from surface to 300 hPa and 700-hPa temperature T (light blue with red edges) from WRF and ERA5 reanalysis data (Fig. S2) over the inner domain (Fig. 1) for the four composite synoptic SOM patterns.

pattern was primarily observed in January (230 h) and March (337 h) and occasionally in February (81 h). The WSWF pattern (Fig. 3d) resembled CSWF (Fig. 3b) in inducing a moist air mass to Payette Mountains. However, in WSWF, a cyclone was located farther to the northwest, bringing warmer air to Idaho compared to CSWF. Temperatures and IVT range between −7° and −2°C and 75–150 kg m^{-1} s^{-1}, respectively (Fig. 4d). WSWF was mainly observed in March (344 h), followed by February (124 h) and January (84 h).

The SOM patterns for CSWF and WSWF closely resembled the composite maps, as indicated by the high PPCC of 0.91, while CZF and WZF showed PPCC values of 0.77 and 0.86, respectively (Fig. 3). However, PPCC alone did not capture the distinctions between these clusters. To address this, we also examined the SI, which measured the similarity of an object to its cluster compared to other clusters (Fig. 3). CZF, CSWF, and WZF exhibited higher SIs (0.29–0.31), indicating that the SOM model faced challenges in distinguishing the warm southwesterly circulations from the other patterns.

The SOM analysis was based on the coarser-resolution (27 km) ERA5 reanalysis data, representing the synoptic-scale weather pattern over the western United States and parts of the Pacific Ocean. To better analyze mesoscale processes, we subsequently utilized the 900-m WRF Model simulations over Idaho, initiated with ERA5. Our goal was to compare the SOM hours of the ERA5 temperature, geopotential height, and IVT with the SOM hours of the WRF simulations to demonstrate that the WRF simulations, initiated with ERA5, reproduced a similar synoptic scale flow over Idaho (Fig. 4). The differences in domain-averaged IVT between ERA5 and WRF for the four different patterns (CZF, CSWF, WZF, and WSWF) were below 10 kg m^{-1} s^{-1}. Similarly, differences in T at 700 hPa remained below 2°C (Fig. 4 and Fig. S2). These results affirmed the fidelity of the simulated synoptic-scale environmental characteristics, justifying the use of WRF simulations to explore how the synoptic flow patterns and underlying terrain influenced microphysical and thermodynamic processes during SNOWIE, leading to different spatio-temporal precipitation patterns.

b. *Moisture transport and precipitation*

Precipitation amounts and distribution exhibited significant variability among the four SOM patterns (Fig. 5). The highest precipitation rates (PR > 0.4 mm h^{-1}) were found in CSWF and WSWF, which were also characterized by the highest IVT ($\overline{\text{IVT}}$ = 123 kg m^{-1} s^{-1}; IVT$_{max}$ = 187 kg m^{-1} s^{-1}) during southwest flow conditions (Figs. 5b,d). Notably, the maximum PR values (1.8 mm h^{-1} for CSWF and 1 mm h^{-1} for WSWF) were observed on the northwestern upwind slopes over the Payette and Salmon River Mountains (Fig. 1). In the case of CSWF, the most intense PR (>1 mm h^{-1}) occurred on the southwestern slopes of the Payette and Sawtooth Mountains. Conversely, mountain ranges located farther downwind from the prevailing synoptic flow (e.g., Bitterroot, Sawtooth, and Salmon River Mountains; Fig. 1) received minimal precipitation due to precipitation shadow effects. These effects were particularly pronounced in the Bitterroot and Sawtooth Mountains for WZF and Salmon River and Bitterroot Mountains for WSWF. On the other hand, the lowest PR (<0.4 mm h^{-1}) was associated with the lowest IVT of 37 and 60 kg m^{-1} s^{-1} during the zonal flow patterns CZF and WZF (Figs. 5a,c). In these cases, precipitation primarily accumulated in the southeastern mountain ranges of Idaho and the Grand Teton in Wyoming.

The standard deviations in IVT exhibited distinct patterns among the synoptic flow patterns. In the CSWF and WSWF patterns, which were characterized by higher IVT values (ranging from 80 to 120 kg m^{-1} s^{-1}), the standard deviations

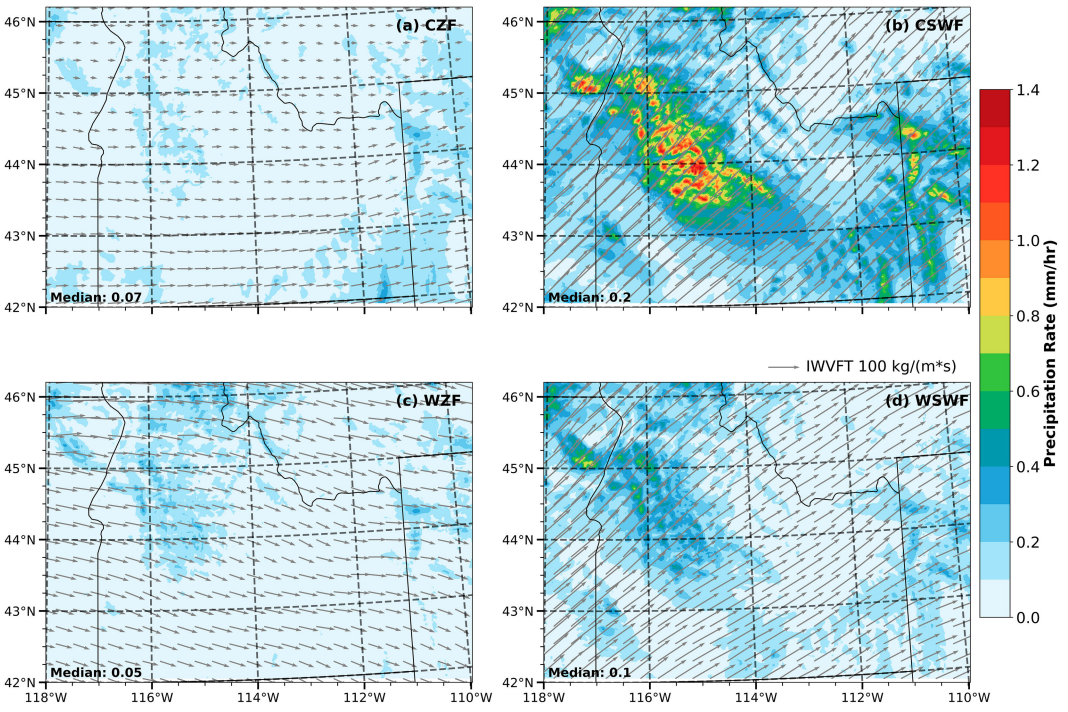

FIG. 5. Mean hourly PR (color coded) and integrated water vapor flux between the surface and 300 hPa (IVT; arrows) based on the 900-m WRF simulations for four synoptic SOM patterns: (a) CZF, (b) CSWF, (c) WZF, and (d) WSWF. State borders are indicated as solid black lines. The median values of PRs are shown in the lower-left corner.

were notably higher (>90 kg m^{-1} s^{-1}). These high-standard deviation areas were primarily situated on the western side of the domain and within the Snake River Valley (Figs. S3b,d). Conversely, over the Payette Mountains and the eastern part of the domain, the standard deviations in IVT decreased to less than 70 kg m^{-1} s^{-1}. In the case of the WZF pattern, a similar spatial pattern was observed compared to CSWF and WSWF, albeit with lower standard deviation values. In this pattern, standard deviations in IVT exceeded 60 kg m^{-1} s^{-1} on the west side of the domain and within the Snake River Valley, while they dropped to less than 55 kg m^{-1} s^{-1} over the Payette Mountains and the eastern portion of the domain (Fig. S3c). Conversely, the CZF pattern exhibited the lowest values in the standard deviation of IVT. In this pattern, higher standard deviations were predominantly present on the southern side of the domain, ranging from 50 to 65 kg m^{-1} s^{-1}, while lower values were observed toward the north, falling below 55 kg m^{-1} s^{-1} (Fig. S3a). In addition, the probability density in IVT showed unimodal patterns for CZF, WZF, and WSWF, peaking around 10, 10–20, and 20 kg m^{-1} s^{-1} correspondingly (Figs. S4a–d). However, in CSWF, it showed bimodal patterns, peaking at 50 and 120 kg m^{-1} s^{-1} (Fig. S4b).

Among the relationship between altitude, temperature, and saturated water vapor pressure, the environmental temperature plays a crucial role in shaping precipitation patterns (Fig. 6). Typically, as altitude increases, temperature decreases, leading to lower saturated water vapor pressure. Consequently, terrain height significantly influences the freezing, condensing, and depositing of water vapor, generally resulting in more precipitation over the higher terrain (Fig. 6). Notably, CZF exhibited widespread snowfall with little rainfall ($S/P > 0.9$; Fig. 6). This pattern was mainly observed in January–February and was associated with the coldest temperatures ($T < -10$°C; Fig. 4). In contrast, CSWF showed a more rapid increase in the proportion of frozen precipitation (S/P) at altitudes below 800 m, with a steady rise between 1000 and 2500 m, peaking at around 0.9 above 2500 m (Fig. 6). Additionally, the precipitation rate steadily increased between 500 and 3500 m, reaching a peak at 0.5 mm h^{-1} (Fig. 6). Interestingly, despite being the second coldest pattern, with most cases occurring in January and February (Fig. 3), CSWF still exhibited a rainfall rate of 0.1 mm h^{-1} at the highest terrain (>3500 m MSL), similar to the rainfall rate observed <1500 m MSL, resulting in an average S/P ratio of 0.7 among the cases. In the cases of WZF and WSWF, frozen precipitation rates increased gradually (<0.1 mm h^{-1}) below 2500 m MSL and then rose to 0.2–0.3 mm h^{-1} above 2500 m MSL. While some rainfall (<0.4 mm h^{-1}) was observed at higher altitudes, most of the precipitation received in elevated terrain was frozen, leading to an increased average S/P ratio to 0.60 (Fig. 6). Overall, the percentage of frozen precipitation increased with altitude. CZF and CSWF exhibited a larger proportion of frozen precipitation than WZF and WSWF due to their favorable temperature conditions, which facilitated the conversion of liquid precipitation and water vapor into ice-phased precipitation while reducing evaporation and melting near the surface.

c. *Integrated ice water path and precipitation patterns*

Integrated IWP, representing the cumulative amount of ice, graupel, and snow, closely correlated with precipitation

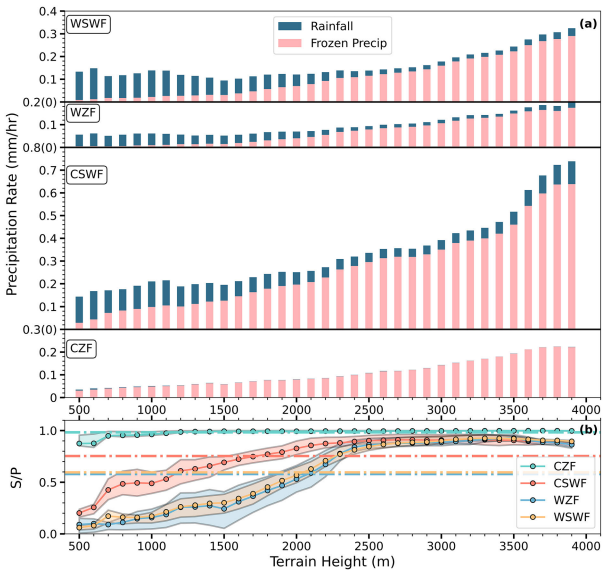

FIG. 6. (a) Domain-averaged PR (mm h^{-1}) and (b) the ratio of frozen (S) to total precipitation (P; rainfall + frozen precipitation) as a function of terrain height for the four SOM patterns. Rainfall is indicated by navy bars and frozen precipitation is indicated by pink bars in (a). Shading indicates the interquartile ranges and dashed-dotted lines represent the average ratio over all terrain heights in (b).

amounts and distribution. Specifically, areas with the highest PR (>0.3 mm h^{-1}) were associated with significant snowfall, as indicated by $S/P > 0.9$ and the highest PR aligned with the highest altitudes (>2.5 km MSL). The magnitude of IWP varied considerably, depending on the IVT and the prevailing synoptic weather pattern. The southwest flow patterns, namely, CSWF (IWP_{max} = 0.8 kg m^{-2}, $\overline{IWP}$ = 0.27 kg m^{-2}; Fig. 7b) and WSWF (IWP_{max} = 0.42 kg m^{-2}, $\overline{IWP}$ = 0.15 kg m^{-2}; Fig. 7d), exhibited the highest IWP values, primarily due to the abundant IVT associated with these patterns. In CSWF, IWP maxima were concentrated around the central Payette Mountains and overlapped with the region of maximum PR. However, there was a slight spatial displacement of precipitation, <10 km, toward the downwind side. This displacement occurred because hydrometeors, as they fell to the ground, were horizontally advected by the mean flow.

Contrary to the correlation between enhanced IWP and enhanced surface precipitation, we also found areas of enhanced IWP that were not correlated with enhanced surface precipitation. For instance, during CSWF and WSWF, areas of enhanced IWP were associated with low PR (<0.1 mm h^{-1}) in the Snake River Valley (IWP > 0.3 kg m^{-2} for CSWF and IWP > 0.2 kg m^{-2} for WSWF). In such cases, we speculated that clouds contained a significant amount of ice particles that were likely too light to reach the ground and the presence of an enhanced updraft prevented the ice from falling to the surface.

The influence of multiple mountain ranges on IWP and surface precipitation was examined over the Salmon River Mountains, comprising three parallel northwest–southeast-oriented mountain ranges: The Lost River Range, the Lemhi Range, and the Beaverhead Mountains (see Fig. 1). During CSWF, and to a lesser extent during WSWF, we observed that IWP > 0.1 mm was associated with PR < 0.1 mm h^{-1} as the air traversed the first mountain range (113.5°W). However, no enhancement in IWP and PR occurred over the subsequent two mountain ranges farther downwind (Lemhi Range and Beaverhead Mountains), suggesting the presence of rain/snow shadow effects. Notably, these shadow effects

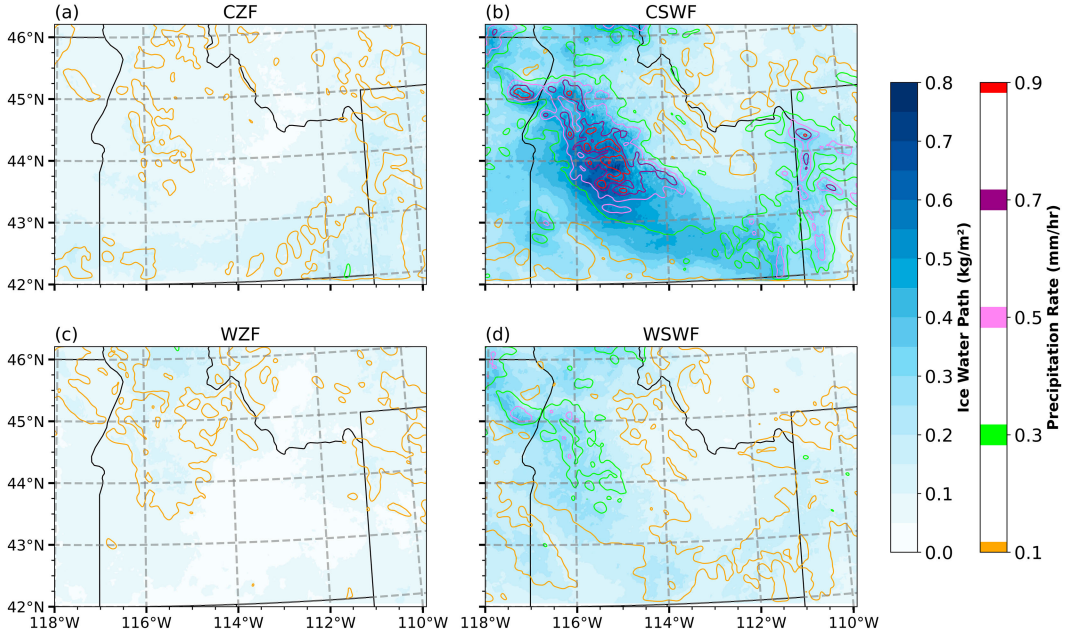

FIG. 7. As in Fig. 5, but showing integrated IWP (ice, snow, and graupel; color shaded) and PR (colored contour line).

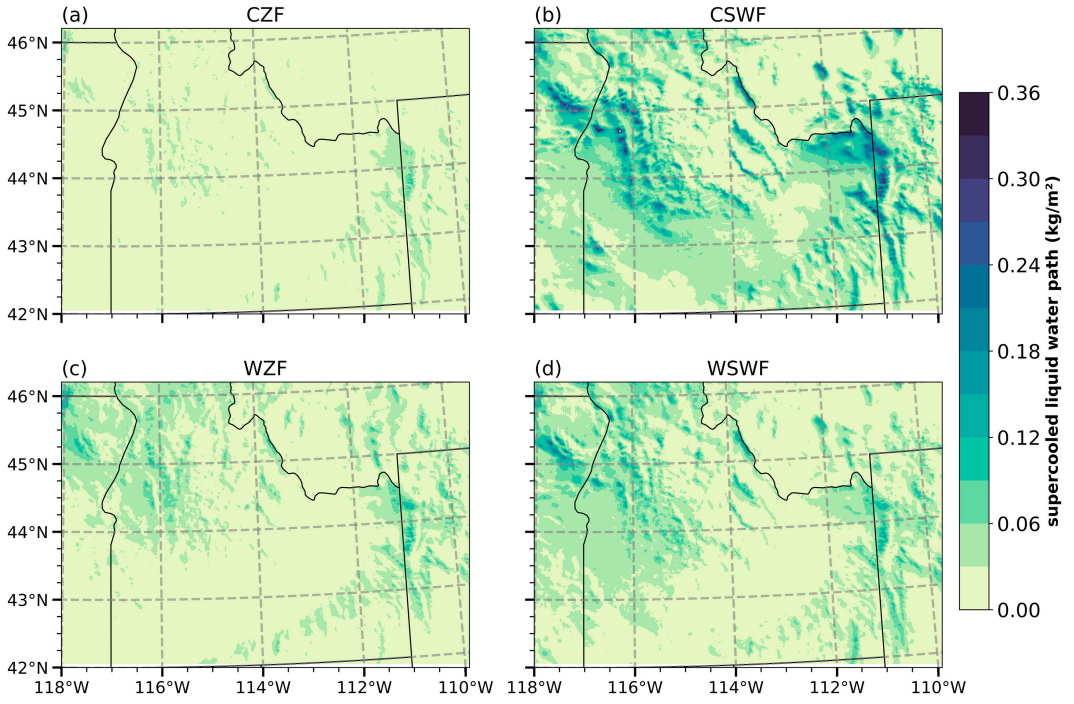

FIG. 8. As in Fig. 5, but showing integrated SLWP (color coded).

were prominent only in the southwesterly flow patterns (WSWF and CSWF) but absent in the zonal flow patterns (CZF and WZF). This discrepancy may be attributed to the difference in the water vapor transport patterns with respect to the orientation of the mountains. In CZF (Fig. 7a), the majority of the IWP (>0.1 kg m^{-2}) was concentrated on the Wyoming Ranges, Teton range in Wyoming, and the northern side of the central Payette Mountains, with IWP values ranging from 0.03 to 0.21 kg m^{-2} for CZF and 0.02–0.19 kg m^{-2} for WZF.

Within each SOM node, most significant variations in IWP (>0.5 kg m^{-2}) predominately occurred in CSWF and WSWF patterns, particularly on the west side of the domain and the Snake River Valley. In contrast, during the CZF and WZF patterns, standard deviations in IWP were mostly <0.45 kg m^{-2} (Fig. S5). The probability density in IWP showed similar trends for each SOM node, with values first dropping rapidly and then gradually decreasing to zero (Fig. S6).

Steep mountain slopes have been recognized as regions of elevated SLW (Sassen et al. 1986; Rauber et al. 2019), which can enhance snowfall through seeder–feeder processes. During CSWF, WSWF, and WZF, the enhanced SLWP was associated with the windward side of the mountain ranges (Fig. 8). The central Payette Mountains and the Teton ranges exhibited higher amounts of SLWP (>0.09 kg m^{-2}), while the Snake River Valley had SLWP < 0.06 kg m^{-2}. Notably, CSWF, WSWF, and WZF displayed SLWP values of up to 0.4, 0.27, and 0.16 kg m^{-2}, respectively. In WSWF and CSWF, the northwest–southeast-oriented mountain ranges (Lost River Range, Lemhi Range, and Beaverhead Mountains) exhibited enhanced SLWP (>0.09 kg m^{-2}). Moreover, mountain ranges farther downwind (Grand Teton and Wyoming Ranges) were associated with higher SLWP compared to the upwind ranges, like Payette Mountains and Sawtooth Ranges. Interestingly, the Snake River Valley, which experienced an increase in IWP (Figs. 7b,c), did not display significantly enhanced SLWP, in a low SLWP/IWP ratio. In contrast, during CZF, over 90% of the area had SLWP < 0.02 kg m^{-2}, with only the windward side of the Grand Tetons, featuring elevations of up to 3500 m MSL, showing SLWP > 0.03 kg m^{-2}. Significant fluctuations in the SLWP were primarily linked to elevated terrain (Fig. S7). In CSWF and WSWF, the standard deviation in SLWP reached its maxima at 0.3–0.45 kg m^{-2}. Meanwhile, in CZF and WZF, higher standard deviations in SLWP were still correlated with mountain summits, with the SLWP standard deviation peaking at 0.2–0.3 kg m^{-2} for WZF and around 0.15 kg m^{-2} for CZF (Fig. S7). The probability density function in SLWP exhibited similar behavior for each SOM node. The values dropped rapidly before gradually decreasing to zero (Fig. S8).

The amount of supercooled liquid and ice within mixed-phased clouds plays a critical role in determining the type and intensity of precipitation (Bergeron 1935; Fan et al. 2017; Pravia-Sarabia et al. 2023). The ratio of SLWP to total hydrometeors path (SLWP + IWP), referred to as SLWR, provided insights into whether clouds were primarily composed of water with a lack of ice particles (SLWR ~ 1) or dominated by ice particles with limited liquid water (SLWR ~ 0; Fig. 9). CSWF and WSWF exhibited elevated SLWR values over the western mountain ranges of the Payette Mountains (Salmon River Mountains and Sawtooth Range) and at higher elevations such as the Grand Tetons (SLWR ~ 0.6; Fig. 9) as well

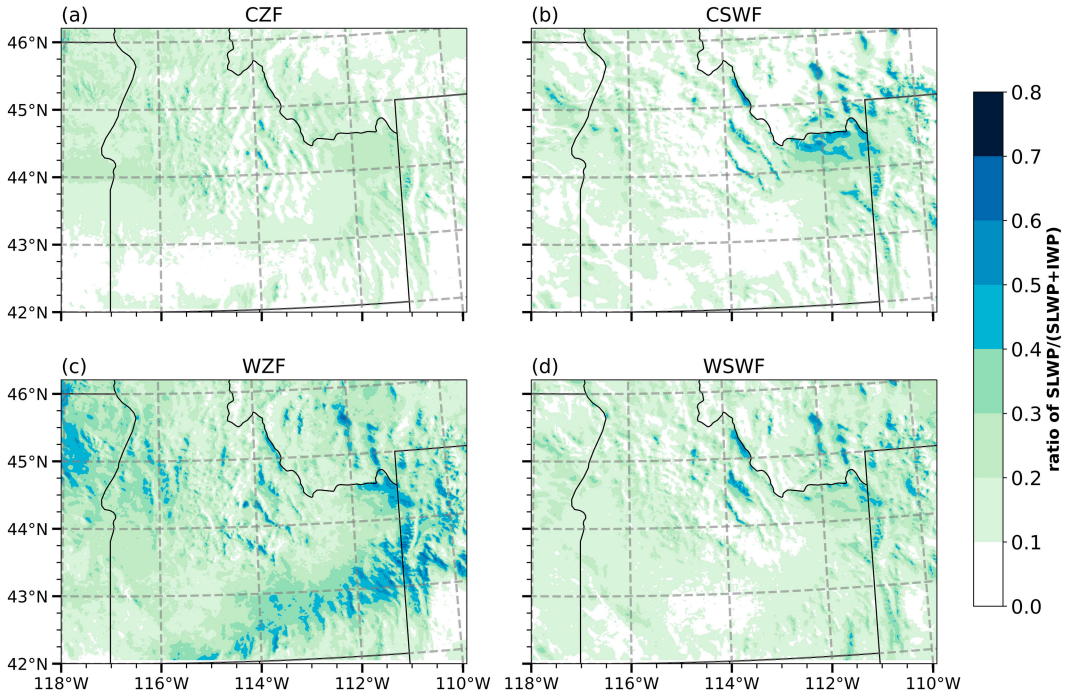

FIG. 9. As in Fig. 5, but showing the ratio of SLWP and SLWP + IWP (color coded).

as the Lost River Range, Lemhi Range, and Beaverhead Mountains (SLWR > 0.5). In contrast, lower SLWRs (<0.2) were predominately found in mountain valleys and within the Snake River Valley. The high values of SLWR associated with low PRs in the Snake River Valley, especially in WZF, were probably due to the frequent occurrence of nonprecipitating supercooled liquid clouds, a phenomenon often observed in satellite data (Fig. 4 in Morrison et al. 2013). Interestingly, domain-averaged SLWR for WZF was larger (SLWR = 0.24) than for CSWF (SLWR = 0.13) and WSWF (SLWR = 0.17). This difference in SLWR and SLWP may be attributed to the use of column-integrated values, which might not accurately reflect the amounts of liquid hydrometeors surpassing the amounts of frozen hydrometeors at a specific location. To address this matter, further investigation and discussion on the vertical distribution of hydrometeors were carried out in the following sections.

To gain a better understanding of the microphysical processes involving diffusional growth, riming, or seeder–feeder mechanisms, we analyzed primary cloud top temperatures (CTTs, Fig. 10) and the vertical distribution of frozen and liquid particles between −40° and 10°C (Fig. 11). CZF and CSWF were associated with colder clouds, as CTT spanned from −25° to −5°C and from −21° to 0°C, respectively (Figs. 10a,b). The CTT in WZF ranged from −16° to 0°C. The coldest clouds ($CTT_{min} \approx -16$°C) were situated in the intersection between Rocky Mountain and Teton Range, while the warmest clouds ($CTT_{max} \approx 0$°C) were found in Snake River Valley. The largest supercooled liquid water fraction (SLWR > 0.5, Fig. 9c) was primarily found in the Teton Range and Wyoming Range (−12 < CTT < −4°C). WSWF, to a larger extent, showed a similar distribution of CTT with that in WZF, ranging from −15° to 3°C. Although WSWF had warmer clouds than WZF, it did not lead to a higher SLWR. This was because WSWF had larger IWP (Figs. 7c,d), making the fraction of supercooled liquid water smaller than WZF (Figs. 9c,d). Therefore, in WSWF, we speculate more ice was not suspended in the warmer primary/lower-lying clouds but rather above the primary/lower-lying clouds, forming "seeder" clouds with abundant ice. This inference could be farther verified by analyzing the vertical distributions of liquid-phased and ice-phased hydrometeors.

The layer-averaged mixing ratio was defined as the mean value of the mixing ratio of a specific hydrometeor within the 2°C temperature range. Below −20°C, the layer-averaged cloud ice mixing ratio (QICEL) increased with decreasing temperatures in all patterns. Among the different weather patterns, CSWF had the highest QICEL, reaching up to 0.002 g kg^{-1}, followed by WSWF with QICEL < 0.0012 g kg^{-1}. CZF and WZF exhibited even lower QICEL, generally < 0.001 g kg^{-1} (Fig. 11a).

The mixing ratios for snow (QSNOW; Fig. 11b), graupel (QGRAP; Fig. 11c), cloud water (QCLOUD; Fig. 11d), and rain (QRAIN; Fig. 11e) all showed a unimodal shape. QSNOW peaked at around −2°C for WZF, −8°C for CZF, −6°C for WSWF, and −6°C for CSWF. These peaks mostly fell within the riming/splintering layer between −3° and −6°C (Hallett and Mossop 1974). This suggests that riming/splintering might have played an essential role in determining the size and shape of snowflakes. The greatest increase in the mixing ratio occurred within the dendritic/diffusional growth and riming/splintering layer. The maximum layer-averaged snow mixing ratios ($QSNOWL_{max}$) were 0.045 g kg^{-1} for WZF, 0.058 g kg^{-1} for CZF, 0.095 g kg^{-1} for WSWF, and 0.13 g kg^{-1}

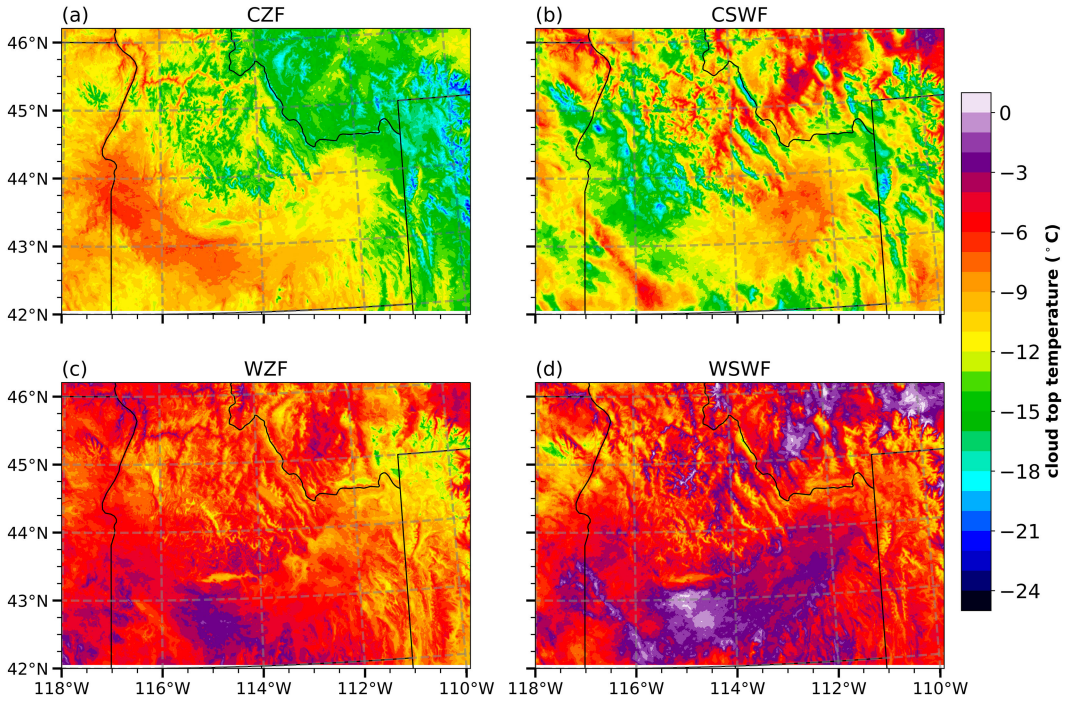

FIG. 10. As in Fig. 5, but showing CTT (color coded).

for CSWF. QGRAP peaked near the freezing point, with values at 0.0045 g kg^{-1} for WZF and 0.000 74–0.0077 g kg^{-1} for CZF, WSWF, and CSWF. Note that in the Thompson–Eidhammer scheme, rimed snow transforms into the graupel when the riming growth rate exceeds the depositional growth rate by a factor of about five (Thompson et al. 2004). Therefore, the increase in QGRAP demonstrated enhanced riming and conversion from snow to graupel, likely resulting in a reduction in the SLW and, consequently, a decrease in QCLOUD between temperatures of 0° and −10°C. Notably, the maximum layer-averaged cloud water mixing ratios (QCLOUDL$_{max}$) were 0.022 g kg^{-1} at −15°C for CZF, 0.058 g kg^{-1} at −10°C for WZF, 0.038 g kg^{-1} at −10°C for CSWF, and 0.04 g kg^{-1} at −8°C for WSWF. This suggests that the WZF had the largest amounts of QCLOUD favoring ice particle growth. In terms of the QRAIN profile, WZF and WSWF displayed higher peak values (QRAINL$_{max}$ ≈ 0.030 g kg^{-1} and QRAINL$_{max}$ ≈ 0.025 g kg^{-1}, respectively) compared to CZF (QRAINL$_{max}$ ≈ 0.023 g kg^{-1}) and CSWF (QRAINL$_{max}$ ≈ 0.007 g kg^{-1}).

The efficiency of the seeder–feeder process relies on the presence of abundant ice and SLW. In the context of glaciogenic cloud seeding, the most substantial seeding impacts are expected in mixed-phased clouds with abundant SLW and low natural ice. WSWF and CSWF appear to favor natural seeder–feeder mechanisms with enhanced QICE, QSNOW, QGRAUP, and QRAIN at $T < 0$°C. Conversely, CZF exhibited the lowest values *of* QRAIN, QGRAUP, and QCLOUD, indicating a deficiency of both SLW and IWC, hindering efficient cloud droplet and precipitation growth. Notably, while the WZF exhibited the highest QCLOUD values at $T < 0$°C, it also had the least amount of snow in the dendritic growth and riming layers. Therefore, WZF might present the most suitable scenario for glaciogenic seeding due to the relatively low efficiency of natural seeder–feeder effects, but abundant supercooled droplets suspended in the clouds.

SLW is often associated with terrain-induced dynamics such as enhanced updraft generated by gravity waves (Reinking et al. 2000; Bruintjes et al. 1994), turbulent eddies near the mountain surface (Lee 1988; Geerts et al. 2011; Chu et al. 2018), and orographic lift along steep terrain (Sassen et al. 1986; Rauber et al. 2019). Therefore, in the next section, we will investigate how vertical velocity and turbulence are linked to the distribution of ice and liquid water and their impact on surface precipitation.

d. *Vertical velocity*

Orographic lifting plays a crucial role in determining precipitation patterns in mountainous regions. When prevailing winds encounter mountain barriers, they are forced to ascend the slopes, undergoing adiabatic cooling. The cooling process leads to the condensation of water vapor and the formation of clouds. Within the planetary boundary layer (<1.5 km AGL), the vertical velocity $W_{pbl} > 0.2$ m s^{-1} was primarily concentrated in mountainous areas, such as the central Idaho mountainous and the Grand Teton Ranges (Fig. 12). In general, larger updrafts in these regions, particular during CSWF and WSWF, where W_{pbl} reached a maximum of ≈ 0.9 m s^{-1}, surpass WZF and CZF, which had updraft capped at about 0.6 m s^{-1}. Downdrafts ($W_{pbl} < 0$ m s^{-1}, Fig. 12) were mainly associated with the ascending flow on the lee side of the mountains. In addition, areas with $W_{pbl} \approx 0$ m s^{-1} (Fig. 12),

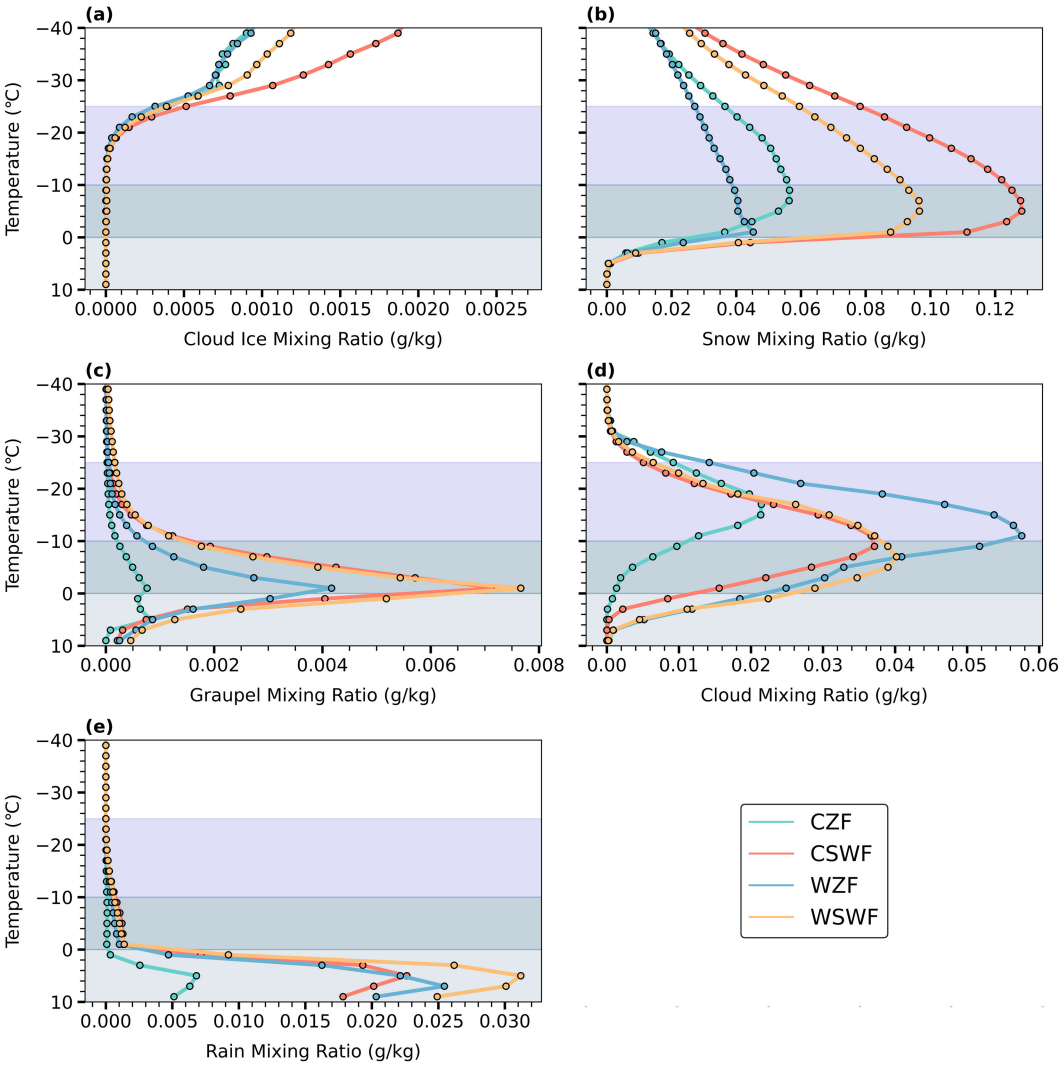

FIG. 11. The domain average of in-cloud mixing ratios of (a) cloud ice, (b) snow, (c) graupel, (d) cloud water, and (e) rain as a function of temperature from the SOM models. In-cloud is where the total hydrometeor mixing ratio (cloud ice + snow + graupel + cloud + rain) $> 10^{-3}$ g kg^{-1}. The shaded background represents the melting layer (light gray color), riming/splintering layer (dark gray color), and dendritic/diffusional growth layer (purple color).

notably in the Snake River Valley, indicated little vertical transport or mixing effects within the boundary layer.

Average upward gradients of equivalent potential temperature within the planetary boundary layer (θ_{e_pbl}) were calculated to reflect the potential instability under different synoptic scenarios. The average $\Delta\theta_{e\_pbl}$ values were 12 K km^{-1} for CZF, 7 K km^{-1} for CSWF, 14 K km^{-1} for WZF, and 10 K km^{-1} for WSWF (Fig. S9). The proportions of gridded points with negative gradients, where θ_{e_pbl} decreases with height, were 15%, 18%, 23%, and 29% for CZF, CSWF, WZF, and WSWF, respectively (Fig. S9). However, the potential instability did not necessarily result in convective updrafts. In mountainous regions, the terrain-induced ascent can be owing to mechanical (airflow over or around an obstacle) and/or thermal (differential heating over sloping terrain) forcing (Kirshbaum et al. 2018). The calculated Pearson correlation coefficients (close to 0; Fig. S10) demonstrated little correlation between convective updrafts and potential instability in this area.

Relative humidity within the planetary boundary layer RH_{pbl} varied substantially across the different synoptic patterns. CSWF was associated with the highest RH_{pbl} (>90%) in the Payette Mountain and Sawtooth Mountain Ranges, along with RH_{pbl} ranging between 80% and 90% in the Bitterroot Ranges, the three northwest–southeast-oriented mountain ranges, and the Grand Teton Ranges. Thus, as this near-saturated air was lifted by the terrain-induced updraft, water vapor cooled and condensed, contributing to cloud and precipitation formation.

SLW tends to be most prevalent in clouds where the condensate supply rate exceeds the diffusional growth rate of ice. This phenomenon is often associated with turbulent eddies near the mountain surface (Lee 1988; Geerts et al. 2011;

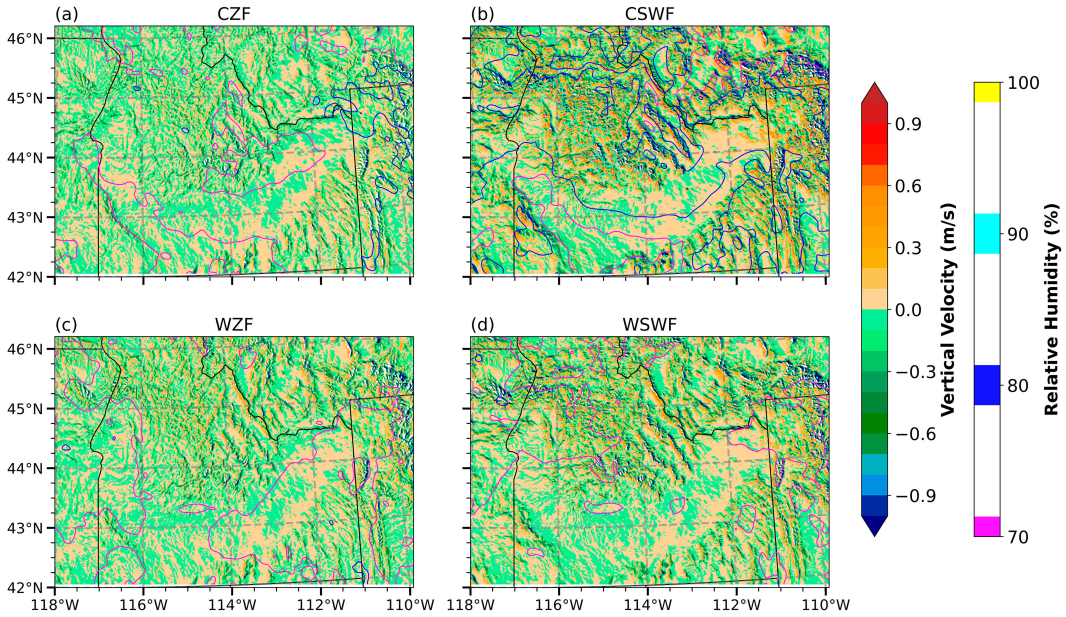

FIG. 12. As in Fig. 5, but showing vertically averaged vertical velocity (shaded color) and relative humidity (colored contour line) within the planetary boundary layer.

Chu et al. 2018). During WSWF, the highest values of turbulent kinetic energy within the planetary boundary layer TKE_{pbl} were found above the highest peaks (>3 km MSL), reaching up to 6 J kg^{-1} (Fig. 13b). While the central Idaho mountains primarily exhibited enhanced TKE_{pbl} (>2 J kg^{-1}; Figs. 13b,d) during CSWF and WSWF, substantial TKE_{pbl} (>2 J kg^{-1}) occurred downstream of the Teton and Wyoming Ranges in all SOM patterns. Conversely, the Snake River Valley and other mountain valleys consistently displayed relatively low TKE_{pbl} (<1 J kg^{-1}) values in all SOM patterns.

A prime example of orographic turbulence enhancement can be seen in the three northwest–southeast-oriented mountain ranges, namely, the Lost River Range, Lemhi Range, and Beaverhead Mountains. In CZF, CSWF, WZF, and WSWF, these ranges exhibited a distinct pattern of staggered high-and-low TKE_{pbl} patterns, with higher values above the ridges and lower values in the valley (Fig. 13). For all SOM patterns, mountain ridges were often associated with higher TKE values due to mountain-induced turbulence resulting most likely from a combination of orographic lift, wind shear, lee waves, or Kelvin–Helmholtz instabilities. Additionally, the rough mountain terrain might lead to more prominent wind shear or vortices on the windward side, contributing to increased turbulent kinetic energy (Lee 1988; Geerts et al. 2011; Chu et al. 2018). On the lee side of the mountain, terrain-induced waves and large eddies can be found. During SW flow conditions (CSWF and WSWF), TKE_{pbl} values exceeding 1.5 J kg^{-1} occurred in the lee of the major ridges, indicating the presence of mountain-induced turbulence (Figs. 13b,d). However, within the valleys, due to the descending motion and the warming caused by compression, stable layer conditions tend to suppress turbulent mixing and dampen turbulence.

To further investigate how the near-surface turbulence and terrain affect surface precipitation, we correlated TKE_{pbl} and PR (Fig. 14). The PCC of TKE_{pbl} and PR ranged between 0.51 and 0.87 (Fig. 14a), primarily indicating the dependence of both variables on elevation. After removing the elevation's influence by detrending (Fig. 14b), PCC < -0.5 for the SW flow was found, while CZF and WZF had PCC values from -0.45 to -0.3 (Fig. 14). CSWF displayed the highest slope and magnitude in TKE_{pbl} and PR compared to CZF, WZF, and WSWF (Fig. 14 yellow lines). All TKE_{pbl} curves exhibited a unimodal shape, with peak values occurring around 2.8 km MSL for all scenarios (CZF, CSWF, WZF, and WSWF). These large values were concentrated in the northeastern corner of the WRF domain (Fig. 1), coinciding with the Rocky Mountains. In addition, despite having slightly lower values of TKE_{pbl} than WSWF, WZF produced the lowest snowfall amount. This suggests that factors beyond turbulent mixing effects, such as enhanced collision-coalescence and broadening of the particle size spectrum, may contribute to the lower efficiency of precipitation in WZF.

4. Conclusions

This study investigated the relationship between synoptic circulation characteristics, mesoscale microphysical and dynamical features, and topography on the surface precipitation over the Payette Mountains of Idaho utilizing the ERA5 dataset and 900-m resolution WRF Model output between January and March 2017, which coincided with SNOWIE. The self-organizing map (SOM) approach was applied to 700-hPa geopotential heights from ERA5 data. The results from the SOM analysis were then applied to a composite analysis using

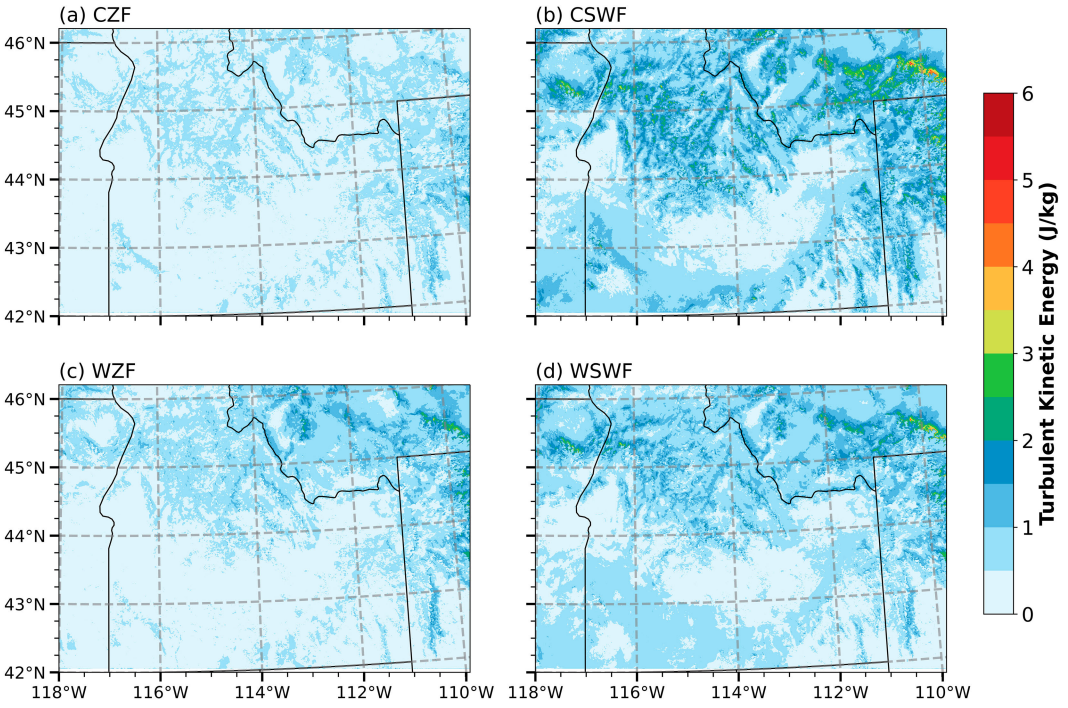

FIG. 13. As in Fig. 5, but showing layer averaged turbulent kinetic energy within the planetary boundary layer (color coded).

the 900-m resolution WRF Model output. This analysis encompassed the distribution of precipitation and integrated hydrometeor path, providing insights into the efficiency of natural precipitation processes and the potential for cloud seeding operations under different synoptic patterns. Furthermore, the study delved into the analysis of the vertical profile of in-cloud hydrometeors within different temperature layers (melting layer, splintering/riming layer, and dendritic/diffusional growth layer). This microphysics perspective shed light on the general features of seeder–feeder processes. The comparison of different underlying topographical features, with particular emphasis on three northwest–southeast-oriented mountain ranges, namely, the Lost River Range, Lemhi Range, and Beaverhead Mountains, highlighted the modulating role of terrains through orographic lifting and turbulent mixing from a dynamic standpoint.

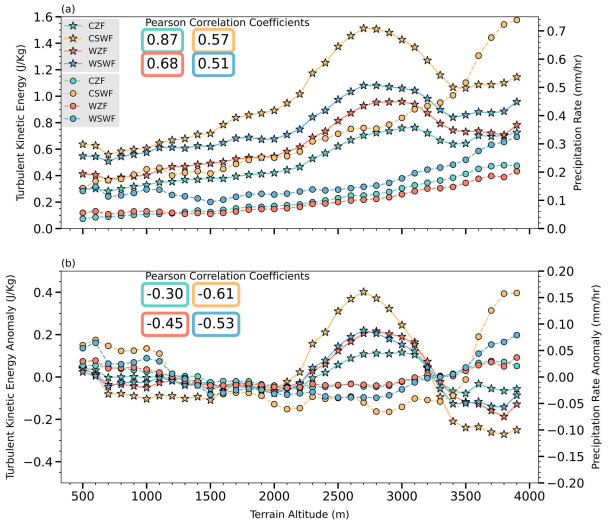

FIG. 14. The domain-averaged precipitation rate (dash line with filled circle symbols) and mean turbulent kinetic energy within the planetary boundary layer TKE_{pbl} (solid line with star symbols) as a function of terrain height for the four SOM models (shown in the legend) for (a) original data and (b) detrended data. The numbers in the colored boxes indicate the PCCs between TKE_{pbl} and PR.

The main conclusions from this study are summarized below:

- Considering the two metrics, SI and PPCC, the 2 × 2 SOM structure had the highest SI value (0.28), while the 5 × 5 SOM structure had the highest PPCC value (0.95). Given the low performance of the 5 × 5 SOM on SI, we selected the 2 × 2 SOM for this analysis.
- Between January and March 2017, WZF was the most frequently observed scenario (30.0%), followed by WSWF (25.5%), CSWF (23.1%), and CZF (21.3%).
- CZF was the scenario with the least amount of IVT (<50 kg m^{-1} s^{-1}), precipitation (PR < 0.4 mm h^{-1}), and SLWP (<0.06 kg m^{-2}). The deficiency in IVT and SLWP resulted in the lowest PRs, and, subsequently, CZF had the lowest cloud seeding potential.
- Spatially, CSWF was associated with the most significant amount of water vapor supplies, SLWP, IWP, and orographic lifting within the boundary layer. Vertically, CSWF had the

highest amount of ice (up to 0.002 g kg^{-1}) located above a high content of SLW (up to 0.038 g kg^{-1}), which favored an efficient natural seeder–feeder process leading to the largest precipitation rates (up to 1.4 mm h^{-1}).
- WSWF shared similar characteristics with CSWF in ground precipitation distribution, integrated ice/supercooled water path distribution, and orographic lifting effect, albeit with lower values of IWP, SLWP, and W_{pbl} compared to CSWF, resulting in the second-largest precipitation rates of up to 0.8 mm h^{-1}.
- WZF had the lowest precipitation rates (PR $<$ 0.4 mm h^{-1}) but featured a significant amount of SLW in the dendritic/diffusional growth layer between $-10°$ and $-25°$C, making this scenario a potential case for glaciogenic cloud seeding operations.
- Complex terrain played an essential role in modulating the local circulation and the distribution of precipitation. The average PR over the Snake River Valley was about 30%–50% lower compared to the Payette Mountains. Higher terrain (>2 km MSL) was usually associated with higher turbulent kinetic energy within the planetary boundary layer ($TKE_{pbl} > 1$ J kg^{-1}), higher vertical velocity ($W_{pbl} > 0.3$ m s^{-1}), and more considerable precipitation rate (PR $>$ 0.1 mm h^{-1}) across all SOM scenarios.

Since only 3 months were investigated in this study, we acknowledge the period of study may not fully represent the general climate patterns. Seasonal snowfall in the American West exhibits significant interannual variability, influenced by factors such as the frequency, intensity, orientation, and landfall location of winter storms. Therefore, it is crucial to expand the scope of our evaluation beyond a single season to capture a more comprehensive picture. Nevertheless, this analysis offers a robust assessment of cloud seeding potential during SNOWIE, providing a basis for comparison with observational analyses. These results should not be taken in a general sense. To do so, this method needs to be applied to multiple years, which we will address in the future.

Acknowledgments. This research was supported by the National Science Foundation (NSF) Grant AGS-2015829. The WRF simulations and subsequent data analysis applied in this paper were completed on the NCAR/CISL HPCs, Cheyenne, and Casper. We thank the anonymous reviewers for their expertise in reviewing this paper; their insightful comments and feedback were greatly appreciated and improved the quality of the paper.

Data availability statement. The simulation data are available through the NCAR campaign data storage upon request (contact: Lulin Xue, xuel@ucar.edu). Codes for data analysis and visualization are available at GitHub (https://github.com/IanXie168/Code_For_Xie_2023).

REFERENCES

American Meteorological Society, 2020: Liquid water path. Glossary of Meteorology, https://glossary.ametsoc.org/wiki/Liquid_water_path.

Baiman, R., A. C. Winters, J. Lenaerts, and C. A. Shields, 2023: Synoptic drivers of atmospheric river induced precipitation near Dronning Maud Land, Antarctica. *J. Geophys. Res. Atmos.*, **128**, e2022JD037859, https://doi.org/10.1029/2022JD037859.

Bergeron, T., 1935: On the physics of clouds and precipitation. *Proc. Fifth Assembly of the Int. Union of Geodesy and Geophysics*, Lisbon, Portugal, UGGI, 156–180.

Bruintjes, R. T., T. L. Clark, and W. D. Hall, 1994: Interactions between topographic airflow and cloud/precipitation development during the passage of a winter storm in Arizona. *J. Atmos. Sci.*, **51**, 48–67, https://doi.org/10.1175/1520-0469(1994)051<0048:IBTAAC>2.0.CO;2.

Cann, M. D., and K. Friedrich, 2020: The role of moisture pathways on snowfall amount and distribution in the Payette Mountains of Idaho. *Mon. Wea. Rev.*, **148**, 2033–2048, https://doi.org/10.1175/MWR-D-19-0350.1.

Cassano, E. N., J. M. Glisan, J. J. Cassano, W. J. Gutowski Jr., and M. W. Seefeldt, 2015: Self-organizing map analysis of widespread temperature extremes in Alaska and Canada. *Climate Res.*, **62**, 199–218, https://doi.org/10.3354/cr01274.

Chu, X., L. Xue, B. Geerts, and B. Kosović, 2018: The impact of boundary layer turbulence on snow growth and precipitation: Idealized large eddy simulations. *Atmos. Res.*, **204**, 54–66, https://doi.org/10.1016/j.atmosres.2018.01.015.

Fan, J., L. R. Leung, D. Rosenfeld, and P. J. Demott, 2017: Effects of cloud condensation nuclei and ice nucleating particles on precipitation processes and supercooled liquid in mixed-phase orographic clouds. *Atmos. Chem. Phys.*, **17**, 1017–1035, https://doi.org/10.5194/acp-17-1017-2017.

Fernández-González, S., F. Valero, J. L. Sánchez, E. Gascón, L. López, E. García-Ortega, and A. Merino, 2015: Analysis of a seeder-feeder and freezing drizzle event. *J. Geophys. Res. Atmos.*, **120**, 3984–3999, https://doi.org/10.1002/2014JD022916.

French, J. R., and Coauthors, 2018: Precipitation formation from orographic cloud seeding. *Proc. Natl. Acad. Sci. USA*, **115**, 1168–1173, https://doi.org/10.1073/pnas.1716995115.

Friedrich, K., and Coauthors, 2020: Quantifying snowfall from orographic cloud seeding. *Proc. Natl. Acad. Sci. USA*, **117**, 5190–5195, https://doi.org/10.1073/pnas.1917204117.

——, and Coauthors, 2021: Microphysical characteristics and evolution of seeded orographic clouds. *J. Appl. Meteor. Climatol.*, **60**, 909–934, https://doi.org/10.1175/JAMC-D-20-0206.1.

Geerts, B., Q. Miao, and Y. Yang, 2011: Boundary layer turbulence and orographic precipitation growth in cold clouds: Evidence from profiling airborne radar data. *J. Atmos. Sci.*, **68**, 2344–2365, https://doi.org/10.1175/JAS-D-10-05009.1.

——, C. Grasmick, R. M. Rauber, T. J. Zaremba, L. Xue, and K. Friedrich, 2023: Vertical motions forced by small-scale terrain and cloud microphysical response in extratropical precipitation systems. *J. Atmos. Sci.*, **80**, 649–669, https://doi.org/10.1175/JAS-D-22-0161.1.

Gibson, P. B., S. E. Perkins-Kirkpatrick, P. Uotila, A. S. Pepler, and L. V. Alexander, 2017: On the use of self-organizing maps for studying climate extremes. *J. Geophys. Res. Atmos.*, **122**, 3891–3903, https://doi.org/10.1002/2016JD026256.

Hallett, J., and S. C. Mossop, 1974: Production of secondary ice particles during the riming process. *Nature*, **249**, 26–28, https://doi.org/10.1038/249026a0.

Han, M., S. A. Braun, T. Matsui, and C. R. Williams, 2013: Evaluation of cloud microphysics schemes in simulations of a winter storm using radar and radiometer measurements. *J. Geophys. Res. Atmos.*, **118**, 1401–1419, https://doi.org/10.1002/jgrd.50115.

Heimes, K., and Coauthors, 2022: Vertical motions in orographic cloud systems over the Payette River Basin. Part III: An evaluation of the impact of transient vertical motions on targeting during orographic cloud seeding operations. *J. Appl. Meteor. Climatol.*, **61**, 1753–1777, https://doi.org/10.1175/JAMC-D-21-0230.1.

Hersbach, H., and Coauthors, 2020: The ERA5 global reanalysis. *Quart. J. Roy. Meteor. Soc.*, **146**, 1999–2049, https://doi.org/10.1002/qj.3803.

Kirshbaum, D. J., B. Adler, N. Kalthoff, C. Barthlott, and S. Serafin, 2018: Moist orographic convection: Physical mechanisms and links to surface-exchange processes. *Atmosphere*, **9**, 80, https://doi.org/10.3390/atmos9030080.

Kohonen, T., 1990: The self-organizing map. *Proc. IEEE*, **78**, 1464–1480, https://doi.org/10.1109/5.58325.

Lee, T. F., 1988: Winter diurnal trends of Sierra Nevada supercooled liquid water and precipitation. *J. Appl. Meteor.*, **27**, 458–472, https://doi.org/10.1175/1520-0450(1988)027<0458:WDTOSN>2.0.CO;2.

Lehner, M., and M. W. Rotach, 2018: Current challenges in understanding and predicting transport and exchange in the atmosphere over mountainous terrain. *Atmosphere*, **9**, 276, https://doi.org/10.3390/atmos9070276.

Lin, Y.-L., 2007: Dynamics of orographic precipitation. *Mesoscale Dynamics*, Y.-L. Lin, Ed., Cambridge University Press, 442–488.

Mazzetti, T., B. Geerts, and L. Xue, 2023: A numerical evaluation of the impact of operational ground-based glaciogenic cloud seeding on precipitation over the Wind River Range, Wyoming. *J. Appl. Meteor. Climatol.*, **62**, 489–510, https://doi.org/10.1175/JAMC-D-22-0132.1.

Mazzetti, T. O., B. Geerts, L. Xue, S. Tessendorf, C. Weeks, and Y. Wang, 2021: Potential for ground-based glaciogenic cloud seeding over mountains in the interior western United States and anticipated changes in a warmer climate. *J. Appl. Meteor. Climatol.*, **60**, 1245–1263, https://doi.org/10.1175/JAMC-D-20-0288.1.

Morrison, A. E., S. T. Siems, and M. J. Manton, 2013: On a natural environment for glaciogenic cloud seeding. *J. Appl. Meteor. Climatol.*, **52**, 1097–1104, https://doi.org/10.1175/JAMC-D-12-0108.1.

Napoli, A., A. Crespi, F. Ragone, M. Maugeri, and C. Pasquero, 2019: Variability of orographic enhancement of precipitation in the Alpine region. *Sci. Rep.*, **9**, 13352, https://doi.org/10.1038/s41598-019-49974-5.

Ohba, M., S. Kadokura, Y. Yoshida, D. Nohara, and Y. Toyoda, 2015: Anomalous weather patterns in relation to heavy precipitation events in Japan during the Baiu season. *J. Hydrometeor.*, **16**, 688–701, https://doi.org/10.1175/JHM-D-14-0124.1.

Pravia-Sarabia, E., J. P. Montávez, A. Halifa-Marin, P. Jiménez-Guerrero, and J. J. Gomez-Navarro, 2023: The role of aerosol concentration on precipitation in a winter extreme mixed-phase system: The case of Storm Filomena. *Remote Sens.*, **15**, 1398, https://doi.org/10.3390/rs15051398.

Purdy, J. C., G. L. Austin, A. W. Seed, and I. D. Cluckie, 2005: Radar evidence of orographic enhancement due to the seeder feeder mechanism. *Meteor. Appl.*, **12**, 199–206, https://doi.org/10.1017/S1350482705001672.

Rauber, R. M., and Coauthors, 2019: Wintertime orographic cloud seeding—A review. *J. Appl. Meteor. Climatol.*, **58**, 2117–2140, https://doi.org/10.1175/JAMC-D-18-0341.1.

Reinking, R. F., J. B. Snider, and J. L. Coen, 2000: Influences of storm-embedded orographic gravity waves on cloud liquid water and precipitation. *J. Appl. Meteor.*, **39**, 733–759, https://doi.org/10.1175/1520-0450(2000)039<0733:IOSEOG>2.0.CO;2.

Rössler, O., P. Froidevaux, U. Börst, R. Rickli, O. Martius, and R. Weingartner, 2014: Retrospective analysis of a nonforecasted rain-on-snow flood in the Alps – A matter of model limitations or unpredictable nature? *Hydrol. Earth Syst. Sci.*, **18**, 2265–2285, https://doi.org/10.5194/hess-18-2265-2014.

Rousseeuw, P. J., 1987: Silhouettes: A graphical aid to the interpretation and validation of cluster analysis. *J. Comput. Appl. Math.*, **20**, 53–65, https://doi.org/10.1016/0377-0427(87)90125-7.

Rutz, J. J., W. J. Steenburgh, and F. M. Ralph, 2015: The inland penetration of atmospheric rivers over western North America: A Lagrangian analysis. *Mon. Wea. Rev.*, **143**, 1924–1944, https://doi.org/10.1175/MWR-D-14-00288.1.

Sassen, K., R. M. Rauber, and J. B. Snider, 1986: Multiple remote sensor observations of supercooled liquid water in a winter storm at Beaver, Utah. *J. Climate Appl. Meteor.*, **25**, 825–834, https://doi.org/10.1175/1520-0450(1986)025<0825:MRSOOS>2.0.CO;2.

Serafin, S., and Coauthors, 2020: *Multi-Scale Transport and Exchange Processes in the Atmosphere over Mountains—Programme and Experiment*. Innsbruck University Press, 42 pp., https://doi.org/10.15203/99106-003-1.

Song, H.-J., and B.-J. Sohn, 2018: An evaluation of WRF microphysics schemes for simulating the warm-type heavy rain over the Korean Peninsula. *Asia-Pac. J. Atmos. Sci.*, **54**, 225–236, https://doi.org/10.1007/s13143-018-0006-2.

Swales, D., M. Alexander, and M. Hughes, 2016: Examining moisture pathways and extreme precipitation in the U.S. Intermountain West using self-organizing maps. *Geophys. Res. Lett.*, **43**, 1727–1735, https://doi.org/10.1002/2015GL067478.

Tessendorf, S. A., and Coauthors, 2019: A transformational approach to winter orographic weather modification research: The SNOWIE Project. *Bull. Amer. Meteor. Soc.*, **100**, 71–92, https://doi.org/10.1175/BAMS-D-17-0152.1.

——, K. Ikeda, C. Weeks, R. Rasmussen, J. Wolff, and L. Xue, 2020: An assessment of winter orographic precipitation and cloud-seeding potential in Wyoming. *J. Appl. Meteor. Climatol.*, **59**, 1217–1238, https://doi.org/10.1175/JAMC-D-19-0219.1.

Thompson, G., and T. Eidhammer, 2014: A study of aerosol impacts on clouds and precipitation development in a large winter cyclone. *J. Atmos. Sci.*, **71**, 3636–3658, https://doi.org/10.1175/JAS-D-13-0305.1.

——, R. M. Rasmussen, and K. Manning, 2004: Explicit forecasts of winter precipitation using an improved bulk microphysics scheme. Part I: Description and sensitivity analysis. *Mon. Wea. Rev.*, **132**, 519–542, https://doi.org/10.1175/1520-0493(2004)132<0519:EFOWPU>2.0.CO;2.

——, P. R. Field, W. D. Hall, and R. M. Rasmussen, 2008: Explicit forecasts of winter precipitation using an improved bulk microphysics scheme. Part II: Implementation of a new snow parameterization. *Mon. Wea. Rev.*, **136**, 5095–5115, https://doi.org/10.1175/2008MWR2387.1.

Udy, D. G., T. R. Vance, A. S. Kiem, N. J. Holbrook, and M. A. J. Curran, 2021: Links between large-scale modes of climate variability and synoptic weather patterns in the southern Indian Ocean. *J. Climate*, **34**, 883–899, https://doi.org/10.1175/JCLI-D-20-0297.1.

Vettigli, G., 2018: Minisom: Minimalistic and NumPy-based implementation of the self-organizing map. Accessed 10 September 2022, https://github.com/JustGlowing/minisom/.

Wang, D., and Coauthors, 2022: Linking synoptic patterns to cloud properties and local circulations over southeastern

Texas. *J. Geophys. Res. Atmos.*, **127**, e2021JD035920, https://doi.org/10.1029/2021JD035920.

Warms, M., K. Friedrich, L. Xue, S. Tessendorf, and K. Ikeda, 2023: Drivers of snowfall accumulation in the central Idaho mountains using long-term high-resolution WRF simulations. *J. Appl. Meteor. Climatol.*, **62**, 1279–1295, https://doi.org/10.1175/JAMC-D-23-0050.1.

Xue, L., and Coauthors, 2013: Implementation of a silver iodide cloud-seeding parameterization in WRF. Part I: Model description and idealized 2D sensitivity tests. *J. Appl. Meteor. Climatol.*, **52**, 1433–1457, https://doi.org/10.1175/JAMC-D-12-0148.1.

——, and Coauthors, 2022: Comparison between observed and simulated AgI seeding impacts in a well-observed case from the SNOWIE Field Program. *J. Appl. Meteor. Climatol.*, **61**, 345–367, https://doi.org/10.1175/JAMC-D-21-0103.1.

Yang, Y., C. Zhao, Y. Wang, X. Zhao, W. Sun, J. Yang, Z. Ma, and H. Fan, 2021: Multi-source data based investigation of aerosol-cloud interaction over the North China Plain and North of the Yangtze Plain. *J. Geophys. Res. Atmos.*, **126**, e2021JD035609, https://doi.org/10.1029/2021JD035609.

Yu, C.-K., W.-F. Liu, L.-W. Cheng, and C.-Y. Lin, 2022: Mechanisms of valley precipitation enhancement over Da-Tun Mountain. *Mon. Wea. Rev.*, **150**, 1851–1871, https://doi.org/10.1175/MWR-D-21-0195.1.

Zaremba, T. J., and Coauthors, 2022a: Vertical motions in orographic cloud systems over the Payette River basin. Part I: Recovery of vertical motions and their uncertainty from airborne doppler radial velocity measurements. *J. Appl. Meteor. Climatol.*, **61**, 1713–1731, https://doi.org/10.1175/JAMC-D-21-0228.1.

——, and Coauthors, 2022b: Vertical motions in orographic cloud systems over the Payette River basin. Part II: Fixed and transient updrafts and their relationship to forcing. *J. Appl. Meteor. Climatol.*, **61**, 1733–1751, https://doi.org/10.1175/JAMC-D-21-0229.1.

Zhang, S., Y. Chen, Y. Luo, B. Liu, G. Ren, T. Zhou, C. Martinez-Villalobos, and M. Chang, 2022: Revealing the circulation pattern most conducive to precipitation extremes in Henan province of North China. *Geophys. Res. Lett.*, **49**, e2022GL098034, https://doi.org/10.1029/2022GL098034.